Structure characterization and tribological study of magnetron sputtered nanocomposite nc-TiAlV(N, C)/a-C coatings

LUO, Quanshun <http://orcid.org/0000-0003-4102-2129>, WANG, Shun Cai, ZHOU, Zhaoxia and CHEN, Linghao

Structure characterization and tribological study of magnetron sputtered nanocomposite nc-TiAlV(N, C)/a-C coatings

Quanshun Luo[a], Shun Cai Wang[b], Zhaoxia Zhou[c] and Linghao Chen[a]

[a] *Materials and Engineering Research Institute, Sheffield Hallam University, Sheffield, S1 1WB, UK.*

[b] *School of Engineering Sciences, University of Southampton, Southampton, SO17 1BJ, UK;*

[c] *Department of Engineering Materials, University of Sheffield, Sheffield, S1 3JD, UK*

Abstract: Grown by reactive unbalanced magnetron sputtering in a mixed N_2 and CH_4 gaseous medium, heterogeneous nanocomposite coatings in the Ti-Al-V-N-C system show extraordinarily excellent tribological performance of coated machining tools. Using analytical high resolution TEM, EELS, FEG-SEM, XRD, and Raman spectroscopy, this paper reports detailed structural and chemical characterization of the coatings grown at various CH_4: N_2 ratios. Meanwhile, the mechanical and tribological properties were also measured, including hardness, Young's modulus, residual stress and the dry-sliding friction and wear at varying environmental humidity. When CH_4 gas was introduced in the deposition, the structure of the coatings has been found to experience a change from nano-scale TiAlN-VN multilayer architecture to a complex mixture of columnar grains of nc-TiAlV(N,C)/a-C nanocomposites and inter-column network of sp^2-type amorphous carbon. Carbon incorporation and segregation also shows remarkable influence on the columnar growth model by leading to finer grain size. As compared to the carbon-free nitride coating, the nanocomposite coatings showed substantially reduced residual stress owing to the free-carbon precipitation, whereas the coatings maintained comparable hardness to the carbon-free TiAlN/VN. Their tribological properties were found to be strongly dependent on the environment. In humid air at RH > 30%, the coatings showed low friction coefficient less than 0.4 and extremely low wear rate at a scale of $\sim 10^{-17}$ $m^3N^{-1}m^{-1}$.

1. Introduction

Hard coatings of transition metal nitrides (TMN) grown by magnetron sputter deposition are important wear resistant materials. In recent years, several technological advances have been made in the synthesis of multi-functional coatings, such as multicomponent alloying, nano-multilayer designing, and self assembly of nanocomposite structures. In the first, alloying the binary nitride TiN with aluminium and chromium can significantly enhance its oxidation resistance, such as the development of magnetron sputtered metastable $Ti_{0.5}Al_{0.5}N$ coating [1-2]. In the ternary Ti-Al-N system, further increase of the Al content leads not only to increased oxidation resistance, but also to spinodal precipitation of hexagonal AlN nano-phase in the cubic crystalline matrix to form a nanocomposite structure [3]. Secondly, nano-multilayer TiN/VN coatings having the TiN and VN bi-layer thickness within a few nanometers were reported to have superhardness over 50 GPa, a value doubling the hardness of the binary nitride components [4]. The concept of lamellate structure with super hardness and strength was first introduced by Koehler [5]. Up to now, polycrystalline multilayer nitride coatings have been successfully developed to show excellent mechanical properties, wear resistance and good performance in various industrial applications [6-8]. Another model of superhard structure, comprising TMN nano-crystallites and a grain boundary phase of resin-like SiN_x, was first proposed by Veprek and co-workers in the Ti-Si-N system [9-10] and then extended to other systems, such as CrSiN [11] and TiBN [12]. Subsequently comprehensive studies have been carried out on the nanocomposite structure, interface and the hardening mechanisms e.g. in refs. [11-16]. Despite the superhardness and or excellent oxidation resistance, however, most TMN coatings exhibit high friction [17].

Incorporation of carbon during the sputtering growth of TMN coatings can bring about dramatic changes in the structure and properties. Carbon is known to have multiple sp, sp^2 and sp^3 binding characteristic, and thereafter may have a series of different condensed structures having diverse physical and mechanical properties. Considering the fact that carbon coatings, mostly diamond like carbon (DLC), have environment-dependent low friction coefficient, more recently the research interests have been focused in the growth of carbon-containing TMN coatings, such as Ti-N-C [18-21], Ti-Al-N-C [22-24], Zr-N-C [25] and Ti-Si-C-N [26-27], which show both high hardness and environment-dependent low friction. It has been found that a transition from columnar nitride crystallites to a dual-phase structure occurs as a result of the precipitation of free carbon in the coating structure. It is known that many nitride coatings grown by vapour deposition shown columnar structure, where the relationship between the deposition conditions and the coating morphology has been established in several models [28]. When carbon is incorporated, it may partially dissolve in the nitride lattice depending on its solubility, whereas the rest carbon precipitates as a secondary free-carbon phase to form the nanocomposite structure [18-27]. Therefore, the coating growth involves redistribution or segregation of the impinging atoms/ions on the growth front. For a dynamically rough growing surface which often happens in magnetron sputtering deposition, the energy distribution of impinging species depends strongly on the local roughness. In particular, the cone-like column tops receive more incident atoms/ions than the column boundary regions because of the shadowing effect of the latter. Such inhomogeneous energy distribution would influence the structural and chemical characteristics of the carbon phase, such as its crystalline structure, chemical bonding, size and shape, and segregation. Unfortunately, these growth-dependent structural characteristics are less mentioned in previous publications. Up

to date, there is still lack of knowledge about the structure evolution in the sputtering growth of carbon containing composite coatings.

This paper reports experimental findings of the structural characterisation of magnetron sputtered multicomponent TiAlVCN coatings along with mechanical and tribological tests. The coatings were grown by co-sputtering of TiAl and vanadium targets in a mixed gaseous medium of N_2 and CH_4. Previously TiAlN/VN multilayers have been developed as candidate coatings for wear protection of machining tools. The TiAlN/VN was found to have high hardness and toughness, lower dry-sliding friction coefficient than other nitride coatings, and extremely low wear rate [7-8, 29]. By incorporating carbon in the TiAlN/VN, the deposited coating was found to show substantially extended tool lifetime in dry machining a wrought aluminium alloy [30]. Preliminary research indicated that the outstanding performance should be attributed to the carbon-modified structure of the TiAlVCN coatings although detailed understanding was not available [31]. This paper reports comprehensive structural characterisation of the carbon-incorporated TiAlVCN coatings by using analytical and high resolution transmission electron microscopy (TEM) with electron energy loss spectroscopy (EELS), field emission gun scanning electron microscopy (FEG-SEM) energy dispersive X-ray spectroscopy (EDX), X-ray diffraction (XRD) and Raman spectroscopy. The experimental findings reported in this paper are expected to improve the understanding of carbon-TMN nanocomposite coatings regarding the chemical states of carbon and the related phase segregation, which therefore contributes to a better control of the mechanical and tribological properties.

2. Experimental

2.1 Coating deposition

Multicomponent TiAlVCN coatings were grown on hardened and polished high speed steel coupons (M2, nominal chemical compositions in we%: C 0.8, Si 0.3, Mn 0.3, Cr 4.0, Mo 6.0, and V 2.0; hardness HV 7.9 GPa) by unbalanced magnetron (UBM) sputtering using an industrial scale PVD unit, the Hauzer HTC-100-4 system. Two pairs of face-to-face pure vanadium targets and $Ti_{0.5}Al_{0.5}$ targets were employed in the sputtering deposition. After pre-heated to 450 ^{0}C in the vacuum chamber, the samples were etched by mixed vanadium and argon ions when one of the two vanadium targets was operated at cathodic glow discharge mode at -1200 V. Then the system was operated under UBM sputtering mode at a substrate bias voltage of -75V, to grow a VN base layer, 0.4 μm thick, and then the TiAlVCN coating. During the TiAlVCN deposition, carbon was incorporated by introducing a mixed N_2+CH_4+Ar atmosphere with separately controlled N_2 and CH_4 fluxes. By adjusting the inletting gas fluxes to make the N_2 to CH_4 ratios to be 3:1, 2:1 and 1:1 in a rank of increasing CH_4 incorporation, three versions of TiAlVCN coatings were grown, namely TiAlVCN-1, TiAlVCN-2 and TiAlVCN-3 as shown in Table 1. The total coating thickness was 3.0 – 3.2 μm as determined using the calotest method.

2.2 Mechanical and tribological tests

A Mitutoyo MVK-H2 Knoop hardness tester was used for coating hardness measurements. The applied indenting load was 25 g, making the indenting depth less than 10% of the coating thickness.

A Fischerscope H100 depth-sensitive indentation tester was used to measure the Young's modulus at an indentation load of 50 mN. The E values were calculated by following the Oliver-Pharr model [32].

Table 1 Chemical composition, Young's modulus and hardness of the investigated materials

	Composition [at%]					E	$HK_{0.025}$
	C	N	Al	Ti	V	[GPa]	[GPa]
TiAlVCN-1	3.12	39.71	13.02	15.21	28.94	335.3 ± 27.0	29.3 ± 0.7
TiAlVCN-2	5.61	38.51	11.66	14.69	29.53	296.9 ± 32.6	28.1 ± 1.4
TiAlVCN-3	6.20	39.07	12.44	14.50	27.78	181.2 ± 14.1	9.9 ± 1.1
TiAlN/VN	-	38.63	14.36	17.08	29.94	417.0 ± 13.7	37.2 ± 2.6
C/Cr	C: 31.49		Cr: 68.51			212.3 ± 1.6	11.9 ± 1.6

A room-temperature ball-on-disk tribometer was employed to investigate the friction and wear properties at ambient conditions. The applied tribo-test conditions were: applied normal load of 5 N, linear sliding speed of 0.1 ms^{-1}, a 6 mm diameter alumina ball as the sliding counterface, and a range of atmospheric relative humidity between 18 % and 72 %. Prior to each test, both the disc and ball samples were cleaned with acetone and dried in air. During each tribo-test, the coefficient of friction was continuously acquired to the computer at a preset frequency of 1 Hz to obtain the friction curve and to calculate the steady friction coefficient. After each test, the obtained wear track was scanned using a laser profilometer to measure the wear track cross-section and thereafter to calculate the wear coefficient.

2.3 Characterizations

A FEG-SEM, FEI Nova-200, was employed to observe the coating surfaces. Chemical compositions of the deposited coatings were determined using the attached ultra-thin windowed EDX system. Whereas SEM-EDX is known for its limited precision in analysing light elements, other complementary analyses were applied to determine the carbon and nitrogen. Raman micro-spectroscopy was conducted by employing a Renishaw-2000 Raman System to characterize the substructures of nitride and free carbon in the deposited coatings. The instrument utilizes a HeNe laser with an excitation wavelength of 632.8 nm, allowing a lower spectral limit of 150 cm^{-1} and upper limit of 2,000 cm^{-1}. Spectra were acquired at frequency range of 200 - 1800 cm^{-1} covering the acoustic and optical vibration bands of transition metal nitrides and the disordered and graphite bands of carbon. The crystallography and residual stress were analysed using a Philips X-Pert X-ray diffractometer operating with a Cu K_α radiation source (40 KV and 40 mA, wavelength λ=0.154056 nm). Residual stress measurements were undertaken using the XRD-$\sin^2\psi$ technique optimised in our recent research [33]. The {220} plane of the nitride phase was selected to collect the diffraction peaks at a series of fixed incident angles.

Extensive structure characterizations were carried using analytical and high resolution TEM, including Philips CM20 (200 kV, LaB_6), JEOL 3010 (300 kV, LaB_6), and JEOL 2010F (200 kV, field emission gun) equipped with EELS capability. For the EELS analysis, core loss spectra were acquired to show the C-K, N-K, Ti-$L_{2,3}$ and V-$L_{2,3}$ edges at a routine energy resolution of 1.2 eV. To ensure acquisition from sample areas thin enough to avoid the need for correction of the spectrum

for plural scattering, it was verified that the plasmon intensity was less than one tenth of the zero-loss peak intensity. Cross-sectional TEM samples were prepared by using a Gatan-691 precision ion polishing system operating at 3.0 – 5.0 kV and low sputtering angles of 5^0 – 8^0.

3. Results

3.1 Chemical composition, mechanical and tribological properties

Table 1 lists the chemical compositions, hardness and elastic modulus of the TiAlVCN coatings. The properties of the carbon-free TiAlN/VN coating and a carbon-based C/Cr coating [34] are also listed for reference. The TiAlVCN coatings show similar chemical compositions to the TiAlN/VN except their carbon contents. In the former, carbon incorporation has been detected. However, the EDX determined carbon contents are very low, which might be caused by high mass absorption of low energy X-ray, a well known limitation for SEM-EDX to measure light elements. More characterizations of carbon were carried out using both Raman spectroscopy and TEM-EELS, to be shown later.

Carbon shows remarkable influence on both the hardness and elastic property. The coatings TiAlVCN-1 and TiAlVCN-2, being deposited at the CH_4:N_2 ratios of 1:3 and 1:2 respectively, exhibit hardness and Young's modulus values only slightly lower than the TiAlN/VN. The TiAlVCN-3, grown at a CH_4:N_2 ratio of 1:1, is much softer and with lower elastic modulus, similar to the properties of the C/Cr coating.

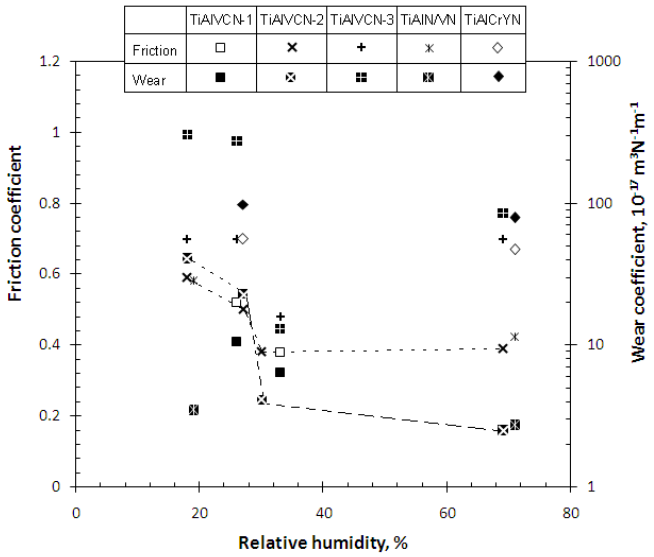

Figure 1 The steady state friction coefficient and wear coefficient of TiAlVCN, TiAlN/VN and TiAlCrYN coatings measured in various environment relative humidity in ball-on-disk sliding tests against an alumina ball counterface.

Figure 1 shows the steady state friction coefficient and wear coefficient of the TiAlVCN coatings measured in a range of relative humidity, RH = 18 - 70 %. The experiment results of two carbon-free coatings, the TiAlN/VN multilayer and the TiAlN based TiAlCrYN, are also included for comparison. All the coatings show environment dependent friction and wear coefficients, having lower friction and lower wear at higher humidity. The TiAlVCN coatings show pronounced dependence of both friction and wear on the environment humidity. The friction coefficients of the TiAlVCN-1 and TiAlVCN-2 coatings are higher than 0.5 and the wear coefficients in the scale of 10^{-16} $m^3N^{-1}m^{-1}$ when the relative humidity is below 30%. A prompt decrease of friction and wear occurs

when the relative humidity increases to 30% and higher, that the friction coefficient becomes less than 0.4 and the wear coefficient reduces to the scale of 10^{-17} $m^3N^{-1}m^{-1}$. In addition, the TiAlVCN-3 coating shows extra-ordinarily high friction and wear. This was caused by the low hardness of the coating triggering severe deformation and abrasive wear. In comparison, the TiAlN/VN coating shows remarkable decrease of friction coefficient from 0.58 to 0.42 with increasing humidity. The wear coefficients of the TiAlN/VN coating are in the scale of 10^{-17} $m^3N^{-1}m^{-1}$, being comparable to previous experiment results [35]. The TiAlCrYN exhibits high friction and wear whereas the variation of humidity shows marginal influence. In brief, the tribological experiments suggest that the incorporation of carbon in the TiAlVCN coatings brings about pronounced environmental-dependence of friction and wear properties as compared to the carbon-free nitride coatings.

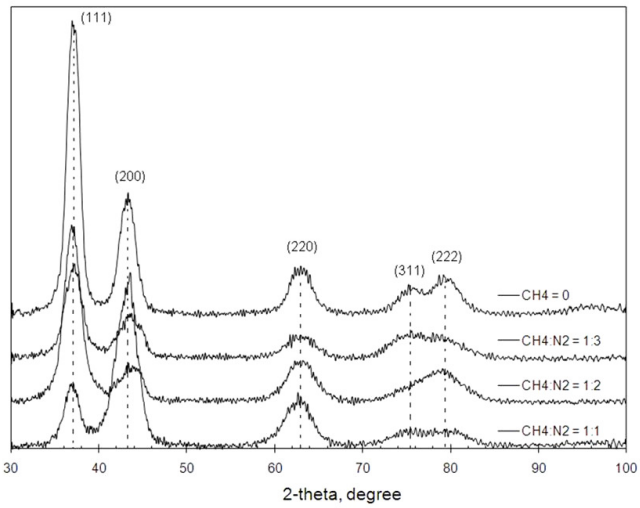

Figure 2 X-ray diffraction curves of the TiAlVCN coatings, with CH_4:N_2 = 1:3, 1:2 and 1:1, and the TiAlN/VN coating (CH_4 = 0).

3.2 Conventional structural characteristics and growth morphology

Figure 2 shows XRD traces of the TiAlVCN and TiAlN/VN coatings. Considering the small coating thickness, the XRD scans were made using a fixed incident angle of $\Omega = 3^0$ whereas the detector scanned over the pre-defined range of 30^0 - 100^0. XRD analysis suggested that the TiAlVCN coatings exhibit NaCl-type cubic crystalline structure, similar to the TiAlN/VN. Precise measurements of residual stress and the stress-free lattice constant were undertaken on the TiAlVCN coatings to compare with the TiAlN/VN. The results are shown in Table 2. The TiAlN/VN coating exhibits high compressive residual stress of -10.06 GPa. In contrast, the residual stress values in the TiAlVCN coatings are lower and dependent on the CH_4:N_2 ratio, from -7.56 GPa in TiAlVCN-1 to -1.34 GPa in TiAlVCN-3. The tress-free lattice constant values of the TiAlVCN coatings, between 0.4161 and 0.4168 nm, are consistent to each other but slightly higher than the constant of TiAlN/VN (0.4107 nm), which account for a difference of 0.0057 nm or a relative variation of 1.39 %. The lattice expansion may indicate partial carbon partition in the TiAlVN nitride to form TiAlN(N,C) carbonitride. In literatures [21-22], similar expansion of the Ti(N,C) phase in a series of carbon-containing TiN coatings provided smaller lattice constant of TiN (a_0 = 0.426 nm) than TiC (a_0 = 0.432 nm).

Table 2 Residual stress and the stress-free lattice parameter.

	Residual stress [GPa]	**Lattice parameter [nm]**
TiAlN/VN	-10.06 ± 2.61	0.4107
TiAlVCN-1	-7.56 ± 0.31	0.4168
TiAlVCN-2	-5.48 ± 0.75	0.4161
TiAlVCN-3	-1.34 ± 0.40	0.4163

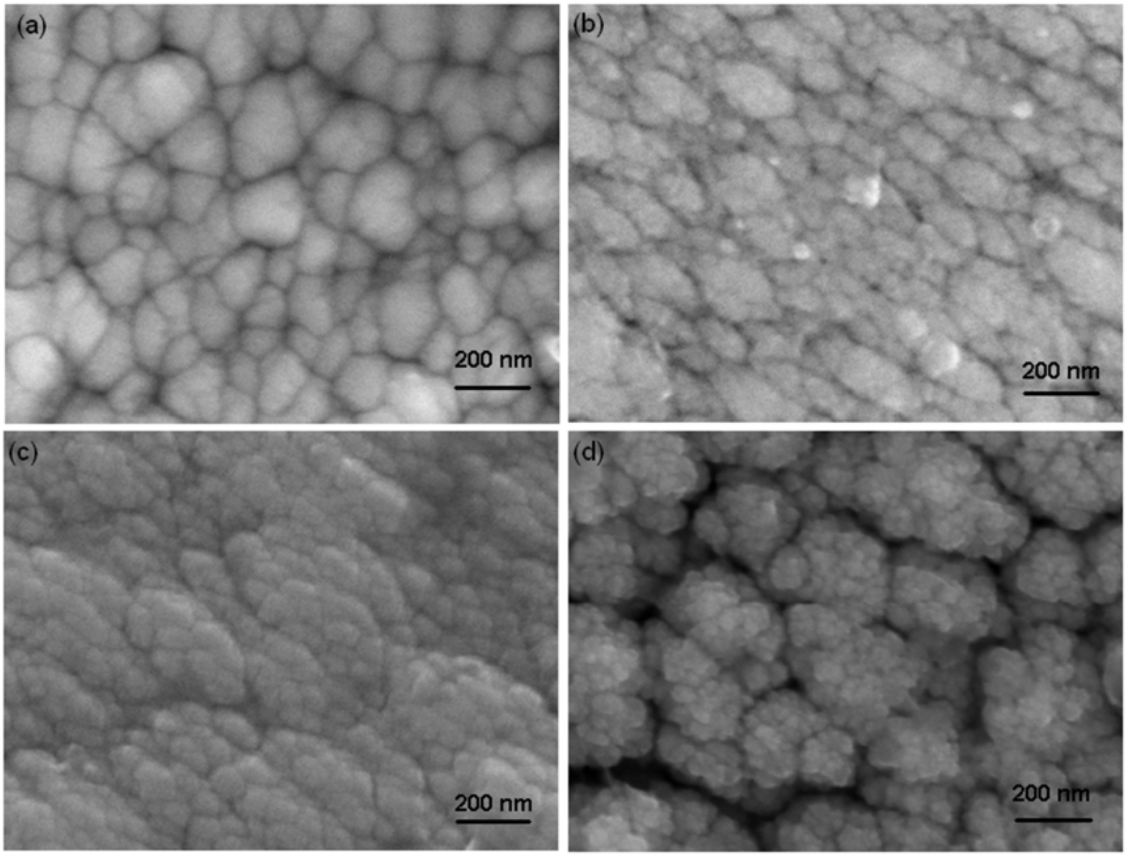

Figure 3 High-resolution SEM images of the TiAlVCN coating surfaces: (a) the TiAlN/VN coating at CH_4 = 0; (b) the TiAlVCN-1 at CH_4:N_2 = 1:3; (c) the TiAlVCN-2 at CH_4:N_2 = 1:2; and (d) the TiAlVCN-4 at CH_4:N_2 = 1:1.

Typical high resolution FEG-SEM images of the TiAlVCN coatings are shown in Figure 3. The coatings exhibit nano-scale rough surfaces having cellular-like topography. According to previous cross-sectional TEM work [36], each cellular cell corresponds to the top of a columnar grain. The carbon-free TiAlN/VN coating shows sub-micron scale surface grain size, Figure 3a. The incorporation of carbon can be found to result in smaller grain sizes down to nano-scale, Figures 3 b-d. In addition, FEG-SEM observations also reveal variation of coating morphology. Whereas the TiAlVCN-1 mainly exhibits reduced grain size as compared to the TiAlN/VN, the TiAlVCN-2 and TiAlVCN-3 coatings show sub-micron scale block cells and each block cell contains up to tens of sub-cells of identical nano-scale size. In particular, the boundaries of the block cells on the TiAlVCN-3 coating surface become valleys, suggesting the formation of sub-dense coating structure. Statistic profile of the cell diameters of the coatings are shown in Figure 4, each having been determined by more than 150 measurements. The TiAlN/VN coating shows a broad range of grain size from 50 to 160 nm. Compared to the TiAlN/VN, all the TiAlVCN coatings exhibit reduced grain sizes depending

on the CH_4:N_2 ratio, i.e. higher CH_4:N_2 ratio refers to smaller grain size. The extreme case was found in the TiAlVCN-3 in which the grain size is about 40 nm only.

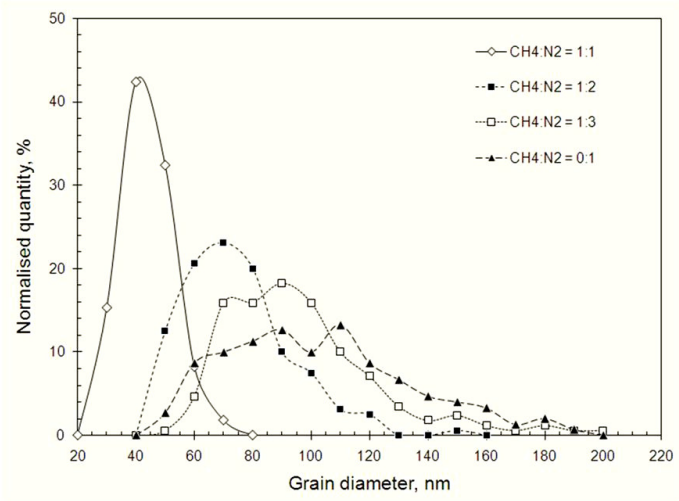

Figure 4 Profile of grain sizes of the TiAlVCN and TiAlN/VN coatings.

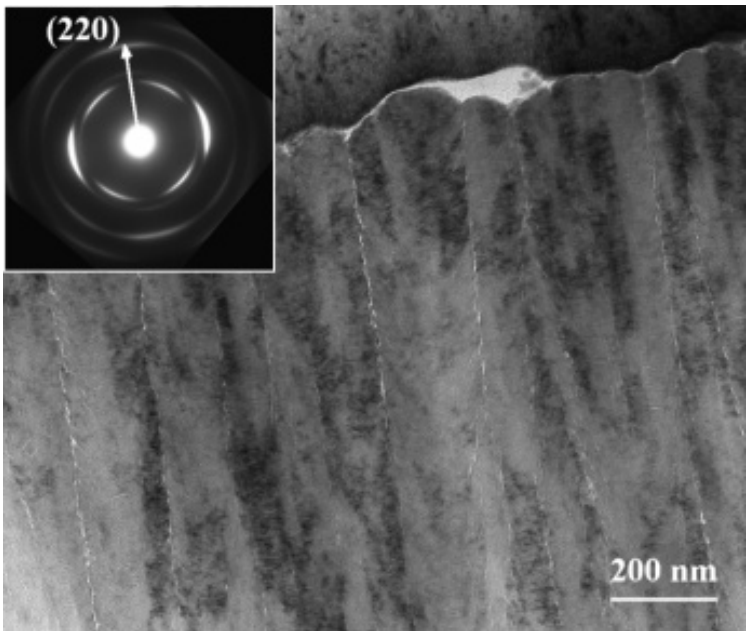

Figure 5 Cross-section TEM BF image of the TiAlVCN-2 coating, showing dense columnar morphology. The inserted SAD pattern suggests its cubic crystalline structure and (220) texture.

Cross-sectional TEM observations indicated that the TiAlVCN coatings have dense columnar structure with sub-dense column boundaries. A typical bright field (BF) TEM image is shown in Figure 5. Selected area diffraction analysis, seeing the pattern inserted in Figure 3, shows strong diffraction arcs of the {111}, {200} and {220} planes of NaCl-type cubic structure, with the {220} diffraction arc being parallel to the growth direction, indicating a strong (220) texture. These characteristics are identical to the carbon-free TiAlN/VN grown under the same conditions. In previous research, we have found that these were related to the low substrate bias voltage of -75V in the UBM sputtering deposition [36].

However, while TiAlN/VN coatings showed nano-scale multilayer fringes in high magnification cross-sectional BF imaging [36], such fringes were not observed in the TiAlVCN coatings. A comparison between the two types of coatings is shown in Figure 6. The TiAlN/VN coating shows typical arch-like multilayer fringes in each column grain, representing mass-difference between the TiAlN (bright) and VN (dark) sub-layers. In the TiAlVCN coating, the BF image shows irregular and

bright lines aligned perpendicular to the growth direction within each column and bright lines along the column boundaries. These bright features should be related to the low-mass matter of free-carbon domains, which has been confirmed in more comprehensive analyses using Raman spectroscopy, high resolution TEM and TEM-EELS analysis.

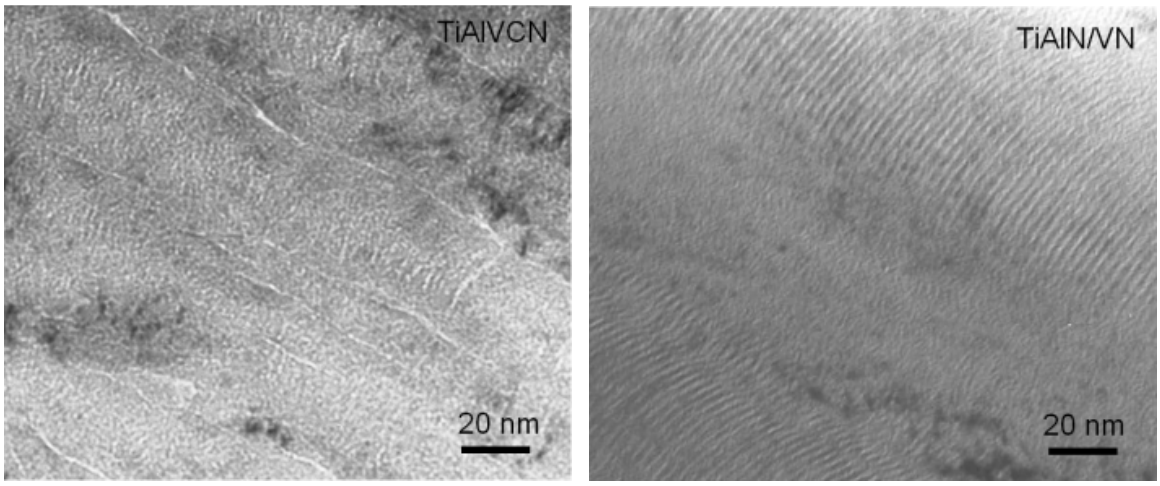

Figure 6 Comparison of cross-sectional TEM BF micrographs of the TiAlVCN and TiAlN/VN coatings, showing different multilayer fringes.

3.3 Raman spectroscopy of carbon-related structural changes

Raman spectroscopic analysis has been carried out on the TiAlVCN coatings grown under various N_2 to CH_4 ratios as well as on the carbon-free TiAlN/VN. Figure 7 shows the overall spectra whereas Figure 8 shows more details of the nitride optical bands and the carbon bands as a function of the CH_4 to N_2 ratio.

The TiAlN/VN coating shows both an acoustic band at 200 – 400 cm^{-1} and an optical band at 550 – 700 cm^{-1}. For transition metal nitrides, Raman spectroscopy detects distortions induced by vacancies, including an acoustic band induced by metal ions and an optical band by non-metal ions [37]. The TiAlVCN coatings also show and acoustic and optical bands from their crystalline nitride components. In addition, the optical bands becomes broader and slightly lower when the CH_4 to N_2 ratio was increased from 1:3 to 1:1, Figure 8. As optical band is induced by vacancies of non-metal ions, this change should be related to the filling-up of some nitrogen vacancies with carbon atoms, i.e. partial solutioning of carbon atoms in the nitride lattice.

Furthermore, the TiAlVCN coatings also show two low broad peaks in the spectra, namely the D (disordered) at 1346 cm^{-1} and G (graphite) bands at 1758 cm^{-1} respectively. The observed D-G bands evidence the presence of free carbon domains. According to [38], the D band arises from the breathing modes of sp^2 atoms in clusters of six-fold aromatic rings, whereas it is forbidden in perfect graphite structure and is only active in disordered carbon. The G band arises from the in-plane bond-stretching motion of pairs of sp^2 carbons of graphite. Thus, the D-G bands in Figure 7 suggest disordered carbon instead of crystalline graphite. Therefore, the TiAlVCN coatings have a composite structure of carbon-containing nitride TiAlV(N,C) and amorphous condensed carbon. Moreover, the volume fraction of free-carbon would be very small for the TiAlVCN coatings grown at the CH_4:N_2 ratios 1:3 and 1:2, which is suggested by comparing the intensities between the

nitride optical band and the D-G bands. When the CH_4 to N_2 ratio was increased to 1:1, the D-G bands are more pronounced than the acoustic and optical bands of the nitride, implying that amorphous carbon became a major component of the coating.

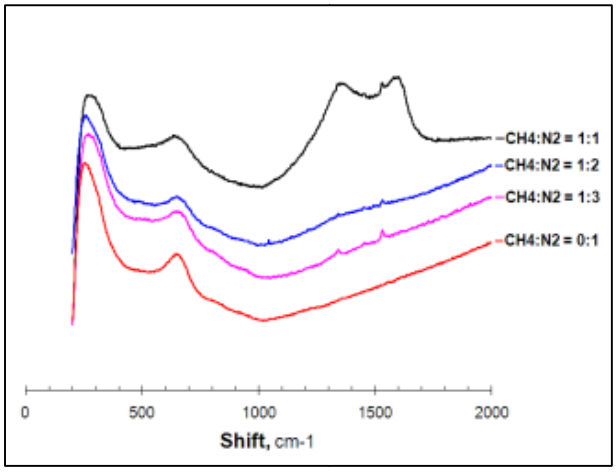

Figure 7 Raman spectra of TiAlN/VN and TiAlVCN coatings.

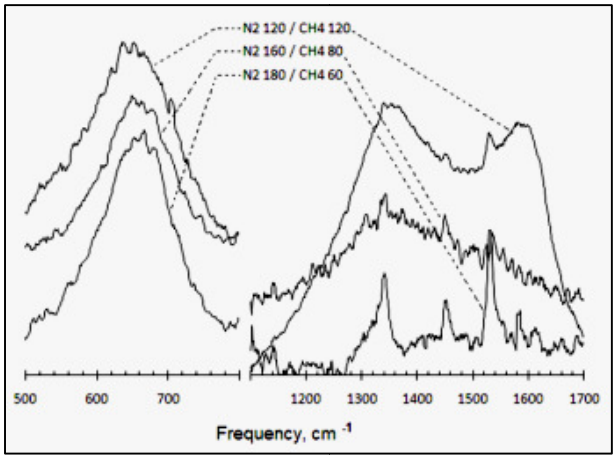

Figure 8 The Raman optical band (500 - 800 cm^{-1}) of nitride and the D-G bands (1100 - 1700 cm^{-1}) of free-carbon compared between the TiAlVCN coatings.

3.4 High resolution TEM of nano-crystalline structure

More details of the composite structure were observed using high resolution TEM at phase contrast imaging. Typical results are shown in Figure 9. In Figure 9a, the TiAlN/VN coating exhibits typical polycrystalline structure with long-range lattices. The observation is similar to the previous high resolution TEM of similar TiAlN/VN coatings [39-40]. The Moire fringes in Figure 9a were caused by overlapping of sub-grains. In Figures 9 b-d, the TiAlVCN-1 and TiAlVCN-2 coatings show mixed structures containing both ordered and disordered regions, which can be identified as crystalline TiAlV(N,C) and amorphous carbon respectively. The amorphous carbon distributes preferentially along the column boundaries and inside the columnar grains. The amorphous carbon inside the columns is nano-scale domains having multilayer-like profile. In Figure 9b, the in-column structure of the TiAlVCN-1 coating comprises TiAlV(N,C) nanocrystallites separated by amorphous carbon. In Figure 9c, the boundary area between two columns is completely disordered and exhibits brighter contrast, suggestive of segregated amorphous carbon. Similar structure was observed in the TiAlVCN-2 sample. In Figure 9d, the two columns exhibit a mixture of crystallite

islands separated by an amorphous medium. The column boundary area is also completely amorphous.

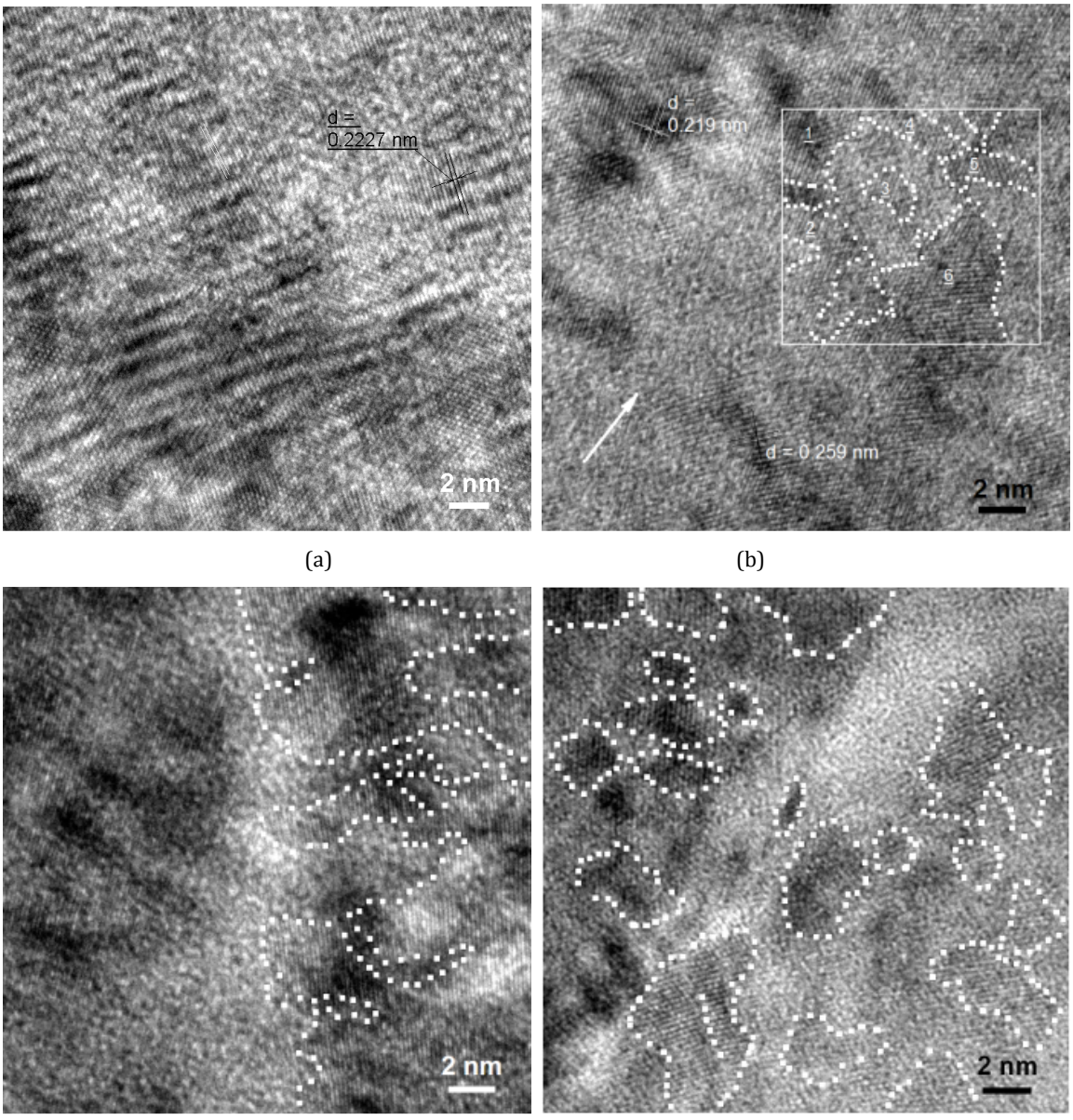

(a) (b)

(c) (d)

Figure 9 Cross-sectional high resolution TEM micrographs: (a) the in-column structure of TiAlN/VN; (b) the in-column structure of TiAlVCN-1, where the coating growth direction is indicated by an arrow; (c) the column boundary area of TiAlVCN-1; and (d) the column boundary area of TiAlVCN-2.

Thus, according to the definition described in literature [9-15, 19-22], the TiAlVCN coatings can be termed as nanocomposites of nc-TiAlV(N,C)/a-C, namely nano-crystalline TiAlV(N,C) and amorphous carbon.

The high resolution TEM observation also provided structure details about the nanocomposition formation. In the first, most of the nano-crystalline domains within each columnar grain exhibit an identical lattice orientation. These nano-crystallites are more like sub-grains of a single columnar grain, instead of randomly oriented crystallites caused by re-nucleation in completely interrupted growth. This finding is important as it evidences that the precipitation of

condensed carbon did not completely block the columnar crystalline growth. Instead, the growth might proceed continuously by rounding over the condensed carbon domains. Such growth agrees with the model suggested in literature [28]. Secondly, the lattice fringes in the obtained high resolution TEM images were measured to calculate the lattice parameters. Similar analyses have been reported by other researchers in [21-22, 39-40]. The results show that, the TiAlVCN-1 and TiAlVCN-2 coatings exhibit lattice constants of 0.449 ± 0.004 and 0.448 ± 0.004 respectively, in which each data was calculated out of nine measurements. The TiAlN/VN coating shows a constant of 0.444 ± 0.004 nm. Again the measured lattice constants of the TiAlVCN coatings are comparable to each other but larger than the TiAlN/VN by 0.96% or 1.17%. This result is consistent with the XRD measurement as shown in Table 2. Obviously, the lattice expansion implies partial substitution of nitrogen ions by the incorporated carbon. In addition, it may be argued that the a_0 values obtained from TEM measurements are systematically high than the XRD measurements (Table 2). However, because identical TEM imaging conditions were applied to all the samples, it is available to reveal the relative variation by comparing the obtained a_0 values.

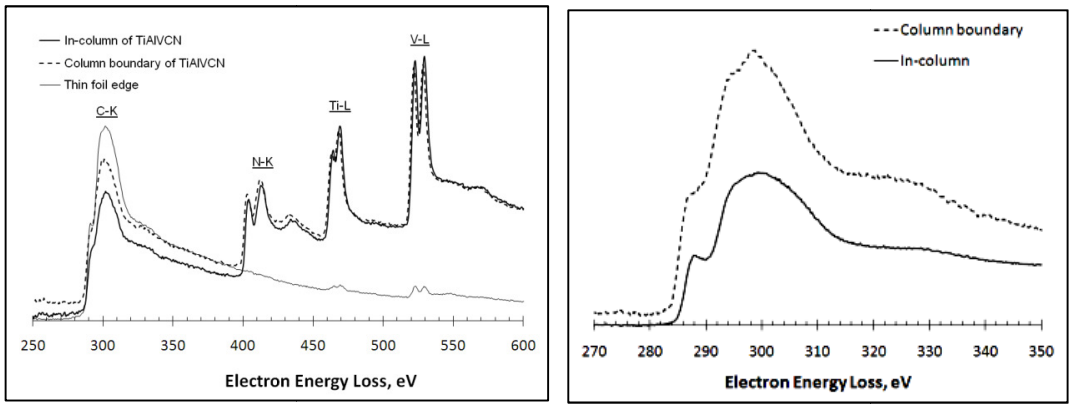

(a) (b)

Figure 10 The Electron energy loss spectra of TiAlVCN coating: (a) The core-loss spectra at 250 – 600 eV; (b) The C-K near edge structure.

Table 3 Energy loss near-edge structure analysis of the TiAlVCN coating: (1) peak positions of the C, N, Ti and V EELS edges; and (2) a comparison of the normalised net peak integrations of the EEL spectra acquired in-column and at column boundary.

	C-K	**N-K**	**Ti-$L_{2,3}$**	**V-$L_{2,3}$**
Energy loss edge [eV]	285.5	398.5	458.8	516.5
Peak positions [eV]	291.5, 301.5	403.5, 412.0, 431.0-438.5	464.0, 468.5	522.5, 529.0
Normalised integration				
Integration window [eV]	279.0 - 307.5	388.0 - 415.5	449.0 - 471.0	508.0 - 531.5
In TiAlVCN column	34%	20%	18%	28%
Column boundary	41%	19%	12%	27%

3.5 TEM-EELS analysis

TEM-EELS analysis has been conducted on typical TiAlVCN samples to explore the structural and chemical characteristics. Spectra were acquired at several areas of the cross-section TEM foil: within a TiAlVCN column grain; at the column boundary region; and at the extremely thin edge with $t/\lambda = 0.19$, where t stands for the foil thickness and λ the mean free past of approximately 100 nm. Figure 10a shows the acquired core loss spectra and Figure 10b provides more details of the C-K

edge. In Figure 10a, the edges of C-K, N-K, Ti-$L_{2,3}$ and V-$L_{2,3}$ are well distinguished from each other. Each edge shows an ionization threshold followed by a well-shaped pattern. The characteristic energy loss values of the edges are summarised in Table 3.

The EELS analysis addresses several findings. In the first, the spectra exhibit almost identical N-K, Ti-$L_{2,3}$ and V-$L_{2,3}$ edges, in terms of energy positions and the edge shapes, as compared to the carbon-free TiAlN/VN coating [41]. In particular, the N-K edge follows the ionization threshold at 398.5 eV consists of two strong and narrow peaks at 403.5 and 412.0 eV and a low and broad peak at 431.0 - 438.5 eV, which are typical features of stoichiometric nitrides. It is known that the energy loss near edge structure (ELNES) can be used as 'fingerprints' to distinguish compounds of similar chemical compositions because it is sensitive to the changes in the local bonding characteristics, coordination and charge distributions of the ionized atoms [42]. Thus, The ELNES of N-K in Figure 10a suggests that the nitride crystallites in the TiAlVCN coatings still remain the stoichiometric cubic structure. This conclusion has good consistence to the Raman spectrospy, XRD and TEM-SAD analyses.

Secondly, the EELS analysis reveals preferential distribution of carbon along the column boundaries. As column boundaries of the TiAlVCN coatings show brighter contrast, e.g. in Figures 6a and 9(c-d), segregation of light elements was suspected to exist there. The two spectra in Figure 10a were acquired in the in-column region and in the column boundary region close to each other, having similar integrated intensities of the C, N, Ti and V edges, to be 1.14 and 1.25 × 10^6 respectively. The similar intensities might indicate comparable sample thickness. Therefore, the net peak integration has been made on the individual edges. The normalised intensities are shown in Table 3, which suggest that the column boundary contains more carbon and less titanium than the in-column region. However, the enriched carbon at column boundary is under-estimated because that the focused electron beam would unavoidably have penetrated into the nc-TiAlV(N,C) column provided that the column boundaries were non-flat and much narrower than the TEM foil thickness (i.e. to be 50 - 80 nm based on zero-loss EELS peak estimation). Nevertheless, the determined carbon enrichment along the column boundary agrees with the TEM BF and high resolution imaging, especially the fully amorphous column boundary.

Thirdly, the ELNES of C-K edge suggests graphite-like structure of the amorphous carbon. In Figure 10b, the C-K edge is featured by an ionization threshold at 285.5 eV and the following components of a broad band around 301.5 eV as well as a small pre-edge resonance at 291.5 eV. The small pre-edge shoulder should correspond to the 1s-π* transition owing to the weak bond of the π electrons. The broad band was attributed to the over-lapping 1s-σ* transitions at the sp, sp^2, and sp^3 sites. The presence of the 1s-π* transition indicates a sp^2-type graphite-like structure of the carbon. On the other hand, the main 1s-σ* transition peaks show feature-less smooth shape, suggestive of amorphous structure. These interpretations are in good consistence to the Raman spectroscopy and HR-TEM observation. More detailed interpretations of EELS C-K edges can be found in literatures [43-46].

Finally, it is noticed that, the edge of the TEM foil exhibits only a strong C-K edge whereas other edges almost disappear. This phenomenon suggests that most of components other than carbon had been sputtered away owing to the difference in the sputtering yields. Sputtering yield is a parameter depending on the characteristics of the solid surface under sputtering and the energy, mass and incident angle of bombarding ions. It was reported that the sputtering yield of carbon accounts for only ~20% of the sputtering yields of Ti and V under Ar-ion bombardment [47].

Consequently, the different sputtering yields resulted in preferential sputtering removal of elements other than carbon during the ion beam milling, which thereafter left an almost pure carbon top layer on the surface of the foil.

4. Discussion

By co-sputtering of TiAl and V targets in a reactive atmosphere of mixed N_2+CH_4+Ar, multicomponent coatings in the Ti-Al-V-N-C system have been grown. In this paper, the influence of carbon incorporation on the formation of nanocomposite structure has been revealed using sophisticated analytical techniques of SEM, XRD, TEM, EELS and Raman spectroscopy. The relationship between the carbon incorporation and the mechanical and tribological properties can be established through the research.

4.1 Nanocomposite structure of the magnetron sputtered TiAlVCN coatings

The structure of the composite coatings can be described in three aspects. In the first, the coatings exhibited dense columnar growth morphology with arch-like growth front and sub-dense column boundaries, NaCl-type cubic crystalline, and strong (220) texture (Figure 5). Such characteristics are identical to the carbon-free TiAlN/VN coatings grown under the same sputtering conditions in exception of the decrease of grain size with increasing CH_4:N_2 ratio. Secondly, when carbon was introduced during the TiAlN/VN deposition, the majority of incorporated carbon atoms has been found to condense as a separate phase of amorphous carbon, distributing either along the column boundaries or inside the columnar grains as nano-scale islands, which has been confirmed by Raman spectroscopic analysis (Figures 4 and 5) and the high resolution TEM (Figure 6). Thirdly, some carbon dissolved in the nitride lattice by occupying some of the octagonal vacancies and or partially replacing nitrogen atoms. The dissolved carbon, forming multicomponent carbonitride TiAlV(N,C), has been found to result in lattice expansion as determined by XRD and HR-TEM (Tables 2 and 3).

Consequently, the coatings exhibited such a three-dimensional nano-structure that, firstly the columnar grains and the inter-column carbon can be termed as ‘columnar nano-structure’; secondly each column exhibits ‘nanocomposite’ of nano-crystallites and nano-scale domains of amorphous carbon. Such nanocomposite structure, being suggested in literature [48], is experimentally reported in the first time.

4.2 Kinetics of nanocomposite structure formation

Before discussing the growth kinetics, it is necessary to clarify three concepts, namely the formation of the columnar morphology, limited solutibility of carbon in transition metal nitride, and the formation of amorphous carbon.

Current research suggests that the coatings grown by UBM sputtering exhibited dense columnar structure and rough surfaces. The growth model was predominantly governed by the low substrate bias voltage with limited mobility of species on the growth front [36]. The incorporation of carbon had been shown to influence the columnar growth by leading to smaller grain size. Moreover, the growth model resulted in preferential distribution of amorphous carbon along the column boundaries.

The limited carbon solubility in metal nitride facilitates accommodation and condensation of carbon atoms at the nitride growth front. In transition metal nitrides, nitrogen occupies the octagonal vacancies. It was reported in literatures [21-22] that, in magnetron sputtered Ti-C-N coatings, increasing nitrogen partial pressure in the deposition of TiC coating led to complete replacing of carbon by nitrogen. On the other hand, however, increasing the partial pressure of gaseous carbon during the deposition of TiN only resulted in limited solutioning of carbon in the nitride. Instead, it triggered the formation of amorphous carbon. This phenomenon was attributed to the stronger binding of nitrogen, than carbon, to metal ions. Furthermore, aluminium component in the Ti-Al-V-N-C system was also likely to promote precipitation of amorphous carbon. Literatures [49-50] reported that non-carbide-forming elements like aluminium and nickel in the Ti-Al-C or Ti-Ni-C ternary systems intend to repel carbon atoms/ions out of the carbide lattices to promote condensation of free-carbon. Such repelling effect can be explained by the chemical inertness between carbon and these elements. For the same reason, the chemical inertness was claimed to promise good performance of carbon-coated tools in machining aluminium alloys for the prevention of aluminium adhesive built-up on the cutting edge [17].

Finally, carbon is an element of tetravalent bonding property and can form strong σ-bonds out of its four equivalent hydbridized 2s- and 2p-orbitals. Depending on the degree of hybridization, carbon may form several structures of sp^1 linear chains, sp^2 planar structures, and sp^3 three-dimensional tetrahedral network [51]. In particular, sp^2 bonded carbon is featured by the strong 2-dimentional (in-plane) σ-bonds and the weak inter-plane π-bonds, which has been found not only in crystalline graphite, but also in carbon onion clusters, amorphous carbon, as well as in carbon nano-tubes. According to the Raman spectroscopy and EELS analysis (Figures 7, 8 and 10), the carbon clusters in the nc-TiAlV(N,C)/a-C nanocomposites exhibited sp^2 amorphous structure with both strong σ-bonds and weak π-bonds.

The kinetics of the nc-TiAlV(N,C)/a-C nanocomposite formation can be described below.

Initial growth of TiAlV(N,C) crystallites repelled extra carbon atoms towards the growth front surface to result in a gradually thickened carbon-rich layer or clouds. Such carbon-rich layer was dynamically movable under ion bombarding, and thereafter preferentially filled up the valleys between the cellular-like growing grains and condensed as amorphous carbon with sp^2 hybridizing structure. Carbon-rich layer also accumulated upon the growing column fronts as small islands of amorphous carbon. As a result, these islands partially blocked the continuous growth of the TiAlV(N,C) crystallites. Further crystallization of incident Ti, Al, V and N ions/atoms might take place either by epitaxial growth rounding over the condensed carbon islands, or by forming new nucleus of TiAlV(N,C) upon these islands. It was more likely that the epitaxial growth mode dominated the TiAlV(N,C) nano-crystallite formation. Under such mode, the newly formed crystallites should have identical lattice orientation to the parent grains. Interestingly, this is supported both by the TEM-SAD analysis and by the HRTEM observations.

4.3 The mechanical and tribological properties of TiAlVCN coatings

Carbon incorporation, through the formation of sp^2 bonded amorphous structure, has shown significant influence on the mechanical properties and tribological behaviours of the TiAlVCN coatings.

It has been frequently reported that nanocomposite coatings showed superhardness [9-15, 25-27]. The plastic and elastic properties of composite coatings are determined by both the nano-crystallite nitride and the resin-like grain boundaries. In literatures, an important condition of superhardness is that the interfacial phase has to be extremely thin, e.g. a single atomic layer or close [14]. Obviously the coatings investigated in this paper did not meet the condition by showing much thicker a-C in column boundaries. The graphite-like sp^2 chemical structure consists of strong σ-bonds and week π-bonds. In particular, the weak π-bond is responsible for the low hardness and low elastic modulus. Similar hardness properties can be found in other a-C containing coatings [24-25]. For the TiAlVCN coatings grown under low CH_4 flux, their hardness and E modulus were dominated by the major structural component, i.e. the nc-TiAlV(N,C). Importantly, the TiAlVCN coatings exhibit slightly lower hardness and modulus than the carbon-free TiAlN/VN coating, which should be attributed to the 2-dimensional network of amorphous carbon along the column boundaries. Interestingly, this is beneficial to the mechanical property by substantial decrease of the residual compressive stress.

The nc-TiAlV(N,C)/a-C composite coatings show friction and wear properties strongly dependent on the microstructure and the test environment. Given that an alumina ball (estimated hardness 15 GPa) was employed as the sliding counterface, high hardness is an essential requirement for the coating to resist plastic deformation and abrasive wear. Therefore, the coatings grown at low CH_4 to N_2 ratios, which showed high hardness values, exhibited low wear rates, whereas the one grown at high CH_4 to N_2 ratio showed much higher wear rate, Figure 1. The strong dependence of friction and wear on the humidity can be explained by the incorporation of amorphous carbon in the coatings. Many carbon based coatings exhibit strongly environmental dependent friction and wear properties [52-53]. In the sp^2 chemical bonding structure of amorphous carbon, the fourth orbital could make feasible self-adhesion of carbon clusters between themselves, or interactions with environmental species, such as [H-O] molecules in humid air, to weaken self-adhesion. Consequently, a transition from high to low friction was found at approximately RH = 30%. At higher humidity, the wear rate can be even lower than the carbon-free TiAlN/VN. In this research, extensive experimental investigations have been carried out on the friction and wear properties as well as the associated mechanisms. Detailed results will be published in a separate article.

5. Conclusions

1) Multicomponent Ti–Al–V–N–C coatings grown by magnetron sputtering in a controlled mixture of N2 and CH4 exhibited columnar cross-sectional morphology, nano-scale rough surface, NaCl-type cubic polycrystalline structure and (220) texture. The structure of the coatings has been characterised to be a complex architecture of columnar grains of nc-TiAlV(N,C)/a-C nanocomposites and an inter-column network of amorphous carbon. For the phase constituents, the majority of carbon atoms/ions were found to condense as amorphous carbon with graphite-like sp2 chemical bonding, whereas some carbon atoms/ions were dissolved in the TiAlV(N,C) carbonite. Segregation of carbon has been found to play a decisive role in the nanocomposite formation. In the columnar growth, some amorphous carbon condensed on the top of the columnar grains partially covering the front surface, resulting in a composite structure of TiAlV(N, C) nano-crystallites and nano-scale

amorphous carbon domains, whereas the amorphous carbon segregated along the column boundaries, forming a two-dimensional network.

2) The coatings grown at low CH4 : N2 ratios of 1 : 3 and 1 : 2 were dominated by the nc-TiAlV(N,C) crystallites and therefore exhibited high hardness of 29 GPa, only slightly lower than the TiAlN/VN. Their Young's modulus and residual compressive stress were substantially lower than the latter. Their tribological properties were found to be strongly dependent on the environment. In dry air with RH < 30%, they exhibited high friction coefficient at 0.5–0.7 and high wear rate at the scale of 10^{-16} m^3N^{-1} m^{-1}; in humid air with RH >30%, their friction coefficient decreased to 0.38–0.5 and the wear rate became extremely low, in the scale of 10^{-17} m^3N^{-1} m^{-1}. The coating grown at high CH_4 to N_2 ratio of 1 : 1 contained a large amount of amorphous carbon, resulting in much lower hardness and Young's modulus, and thereafter triggering higher wear rate by several orders of magnitude.

Acknowledgements

Partial financial support from The European Commissions, through the research project (Grant No. GRD1-2001-40514), and from Engineering and Physical Sciences Research Council (EPSRC, UK, Grant No GR/N23998/01) is acknowledged.

References

[1] W. D. Münz, *J. Vac. Sci. Technol.,* 1986, **4**, 2717.
[2] S. Paldeys and S.C. Deevi, Mater. Sci. Eng., 2003, **A342**, 58.
[3] P.H. Mayrhofer, A. Horling, L. Karlsson, J. Sjolen, T. Larsson, C. Mitterer and L. Hultman, *Appl. Phys. Lett.*, 2003, **83**, 2049.
[4] U. Helmersson, S. Todorova, S.A. Barnett, J.E. Sandgren, L.C. Markert and J.E. Greene, *J. Appl. Phys.*, 1987, **62**, 481.
[5] J.S. Koehler, *Phys.* Rev., 1970, **B2**, 547.
[6] X. Chu, M.S. Wong, W.D. Sproul and S.A. Bernett, *J. Mater. Res.*, 1999, **14**, 2500.
[7] W. D. Münz, L. A. Donohue and P. Eh. Hovsepian, *Surf. Coat. Technol.*, 2000, **125**, 269.
[8] P. Eh. Hovsepian, Q. Luo, G. Robinson, M. Pittman, M. Howarth, D. Doerwald, R. Tietema, W.M. Sim and M.R. Stalley, *Surf. Coat. Technol.*, 2006, **201**, 265.
[9] S. Veprek, S. Reiprich and S. Li, *Appl. Phys. Lett.* 1995, **66**, 2640.
[10] M. Kong, W. Zhao, L. Wei and G. Li, *J. Phys. D: Appl. Phys.*, 2007, **40**, 2858.
[11] Q. M. Wang and K. H. Kim, *Acta Mater.*, 2009, **57**, 4974.
[12] J. Neidhardt, Z. Czigany, B. Satory, R. Tessadri, M. O'sullivan and C. Metterer, *Acta Mater.*, 2006, **54**, 4193.
[13] C. Lu, Y.W. Mai and Y.G. Shen, *J. Mater. Sci.*, 2006, **41**, 937.
[14] L. Hultman, J. Bareno, A. Flink, H. Soderberg, K. Larsson, V. Petrova, M. Oden, J. E. Greene and I. Petrov, *Phys. Rev.*, 2007, **B75**, 155437.
[15] R.F. Zhang, A.S. Argon and S. Veprek, *Phys. Rev. Lett.*, 2009, **102**, 015503.
[16] E. Konca,Y.-T. Cheng, A.M. Weiner, J.M. Dasch, A. Erdemir and A.T. Alpas, *Surf. Coat. Technol.*, 2005, **200**, 2260.
[17] M. Lahres, P. Muller-Hummel and O. Doerfel, *Surf. Coat. Technol.*, 1997, **91**, 116.
[18] Y. Cheng and Y.F. Zheng, *Surf. Coat. Technol.*, 2007, **201**, 4909.
[19] D. Martınez-Martınez, C. Lopez-Cartes, A. Justo, A. Fernandez and J.C. Sanchez-Lopez, *Solid State Sciences*, 2009, **11**, 660.
[20] M. Nose, T. Kawabata, S. Khamseh, K. Matsuda, K. Fujii, S. Ikeno and W.A. Chiou, *Mater. Trans.*, 2010, **51**, 282.
[21] Y.H. Lu, J.P. Wang and Y.G. Shen, *Appl. Surf. Sci.*, 2009, **225**, 7858.
[22] Y.H. Lu and Y.G. Shen, *Appl. Phys. Lett.*,2007, **90**, 221913
[23] X. Zhang, J. Jiang, J. Lin and J.J. Moore, *Surf. Coat. Technol.*, 2009, **203**, 3450.
[24] J.M. Lacker, W. Waldhauser, R. Ebner, R.J. Bakker, T. Schoberl and B. Major, *Thin Solid Films*, 2004, **468**, 125.
[25] H.K. Li, G.Q. Lin and C. Dong, *J. Inorganic Materials*, 2010, **25**, 517.

[26] S.L. Ma, D.Y. Ma, Y. Guo, B. Xu, G.Z. Wu, K.W. Xu and P. K. Chu, *Acta Mater.*, 2007, **55**, 6350.
[27] R.H. Wei, *Surf. Coat. Technol.*, 2008, **203**, 538.
[28] P. B. Barna and M. Adamik, *Thin Solid Films*, 1998, **317**, 27.
[29] Q. Luo, P.Eh. Hovsepian, D.B. Lewis, W.-D. Münz, Y.N. Kok, J. Cockrem, M. Bolton and A. Farinotti, *Surf. Coat. Technol.*, 2005, **193**, 39.
[30] P.E. Hovsepian, A.P. Ehiasarian, A. Deeming and C. Schimpt, *Vacuum*, 2008, **82**, 1312.
[31] Q. Luo, C. Schimpt, A.P. Ehiasarian, L. Chen and P. Eh. Hovsepian, *Plasma Process & Polymers*, 2007, **4**, S916.
[32] A. R. Franco Jr., G. Pintaúde, A. Sinatora, C. E. Pinedo and A. P. Tschiptschin, *Mater. Res.*, 2004, **7**, 483.
[33] Q. Luo and A.H. Jones, *Surf. Coat. Technol.*, 2010, **205**, 1403.
[34] P.Eh. Hovsepian, D.B. Lewis, C. Constable, Q. Luo, Y.N. Kok and W.D. Münz, *Surf. Coat. Technol.*, 2003, **174-175**, 762.
[35] D.B. Lewis, S. Creasey, Z. Zhou, J.J. Forsyth, A.P. Ehiasarian, P.Eh. Hovsepian, Q. Luo, W.M. Rainforth and W.D. Münz, *Surf. Coat. Technol.*, 2004, **177-178**, 252.
[36] Q. Luo, D.B. Lewis, P.Eh. Hovsepian and W.D. Münz, *J. Mater. Res.*, 2004, **19**, 1093.
[37] H.C. Barshilia and K.S. Rajam, *J. Mater. Res.* 2004, **19**, 3196.
[38] J.C. Sanchez-Lopez, A. Erdemir, C. Donnet and T.C. Rojas, *Surf. Coat. Technol.*, 2003, **163-164**, 444.
[39] H. Meidia, A.G. Cullis, C. Schonjahn, W.D. Münz and J.M. Rodenburg, *Surf. Coat. Technol.*, 2002, **151-152**, 209.
[40] M. Kong, N. Shao, Y. Dong, J. Yue and G. Li, *Mater. Lett.*, 2006, **60**, 874.
[41] Q. Luo, Z. Zhou, WM. Rainforth and P.Eh. Hovsepian, *Tribo. Lett.*, 2006, **24**, 171.
[42] F. Hofer, P. Warbichler, A. Scott, R. Brydson, I. Galesic and B. Kolbesen, *J. Microscopy*, 2001, **204**, 166.
[43] J.C. Sanchez-Lopez, A. Erdemir, C. Donnet and T.C. Rojas, *Surf. Coat. Technol.*, 2003, **163-164**, 444.
[44] A.P. Merkle, A. Erdemir, O.L. Eryilmaz, J.A. Johnson and L.D. Marks, *Carbon*, 2010, **48**, 587.
[45] L. Ponsonnet, C. Donnet, K. Varlot, J.M. Martin, A. Grill and V. Patel, *Thin Solid Films*, 1998, **319**, 97.
[46] A. Alexandrou, H.-J. Scheibe, C. J. Kiely, A. J. Papworth, G. A. J. Amaratunga and B. Schultrich, *Phys. Rev.*, 1999, **B16**, 10903.
[47] S.L. Rohde, *Sputtering deposition, in ASM Handbooks on-line version, Vol. 5: Surface Engineering*.
[48] J. Musil, *Physical and mechanical properties of hard nanocomposite films prepared by reactive magnetron sputtering, in Nanostructured hard coatings, eds. J.T.M. De Hosson and A. Cavaleiro, Springer Science + Business Media, LCC, New York, NY 10013, U.S.A.,* 2006, 407-463.
[49] M. Lindquist, O.Wilhelmsson, U. Jansson and U.Wiklund, *Wear*, 2009, **266**, 379.
[50] E. Lewin, B. Andre, S. Urbonaite, U. Wiklund and U. Jansson, *J. Mater. Chem.,* 2010, **20**, 5950.
[51] A. Krueger, *Carbon materials and nanotechnology, Wiley-VCH 2010, Weinheim, p6*.
[52] L. Xia and G. Li, *Wear*, 2008, **264**, 1077.
[53] A. Erdemir and C. Donnet, *J. Phys. D: Appl. Phys.*, 2006, **39**, R311.